1 For: bioRxiv, *New Results*

2

3 Complete title: Visualization of Arabidopsis root system architecture in 3D by refraction-

4 contrast X-ray micro-computed tomography

5

6 Running title

7 X-ray micro-CT of Arabidopsis root system

8

9 Authors:

10 Tomofumi Kurogane[1], Daisuke Tamaoki[2], Sachiko Yano[3], Fumiaki Tanigaki[3], Toru

11 Shimazu[4], Haruo Kasahara[5], Daisuke Yamauchi[6], Kentaro Uesugi[7], Masato Hoshino[7],

12 Seiichiro Kamisaka[2], Yoshinobu Mineyuki[6], *Ichirou Karahara[2]

13

14 Address:

15 [1]Graduate School of Science and Engineering for Education, University of Toyama, 3190

16 Gofuku, Toyama 930-8555, Japan, [2]Faculty of Science, University of Toyama, 3190 Gofuku,

17 Toyama 930-8555, Japan, [3]Japan Aerospace Exploration Agency, 2-1-1 Sengen, Tsukuba

18 305-8505, Japan, [4]Japan Space Forum, 3-2-1 Kandasurugadai, Tokyo 101-0062, Japan,

19 [5]Japan Manned Space Systems Corp., 1-1-26 Kawaguchi, Tsuchiura 300-0033, Japan, [6]

20 Graduate School of Life Science, University of Hyogo, 2167 Shosha, Himeji, Hyogo 671-

21 2280, Japan, [7]Japan Synchrotron Radiation Research Institute, 1-1-1 Kouto, Sayo, Sayo-gun,

22 Hyogo 679-5198, Japan

23

24 *To whom correspondence should be addressed.

25 E-mail: karahara@sci.u-toyama.ac.jp

26   Ichirou Karahara

27   Department of Biology, Faculty of Science, University of Toyama, 3190 Gofuku, Toyama

28   930-8555, Japan

29   Tel: + 81-76-445-6630   Fax: + 81-76-445-6549

30

33

34   The total number of pages: 20

35   The total number of figures: 11

36

37

38   **Abstract**

39

40   Plant roots change their morphological traits in order to adapt themselves to different

41   environmental conditions, resulting in alteration of the root system architecture. To

42   understand this mechanism, it is essential to visualize morphology of the entire root system.

43   To reveal effects of long-term alteration of gravity environment on root system development,

44   we have performed an experiment in the International Space Station using Arabidopsis

45   (*Arabidopsis thaliana* (L.) Heynh.) plants and obtained dried root systems grown in rockwool

46   slabs (mineral wool substrate). X-ray computer tomography (CT) technique using an

47   industrial X-ray scanner has been introduced for the purpose to visualize root system

48   architecture of crop species grown in soil in 3D non-invasively. In the case of the present

49   study, however, root system of Arabidopsis is composed of finer roots compared with typical

50   crop plants and rockwool is also composed of fibers having similar dimension to that of the

51   roots. A higher spatial resolution imaging method is required for distinguishing roots from

52   rockwool. Therefore, in the present study, we tested refraction-contrast X-ray micro-CT using

53   coherent X-ray optics available at the beamline BL20B2 of the synchrotron radiation facility

54   SPring-8. Using this technique, both the primary and the secondary roots were successfully

55   identified in the tomographic slices, clearly distinguished from the individual rockwool fibers

56   and resulting in successful tracing of these roots from their basal regions. This newly-

57   developed technique should contribute to elucidate the effect of microgravity on Arabidopsis

58   root system architecture in space.

59

60   **Main text**

61   **Introduction**

3

62 The plant root system, i.e., the belowground part of the plant body, provides a basis of

63 supporting and anchoring the shoot system, i.e., the aboveground part of the plant body, as

64 well as of growth by uptaking water and nutrients from soil. The plant root system adapts

65 itself to surrounding soil environment changing its architecture [1]. This capability of the

66 plant root system is called root system plasticity [2]. Understanding the mechanism of root

67 plasticity is important for optimization of plant cultivation conditions under given

68 environment. Greater root system development under mild drought stress is considered to

69 contribute to their increased dry matter production [3]. Genotypes having increased total root

70 length showed greater shoot dry matter production under mild water deficit condition [4].

71   The first step to understand mechanisms of root plasticity under different

72 environmental stimuli is to precisely describe the morphology of the root system architecture.

73 And the second one is to extract necessary information from it as much as possible. The

74 methodology to analyze the root system architecture is still developing. A widely-used

75 conventional method is to use rhizotron [5], which is to visualize the root system architecture

76 *in situ* in 2D. On the other hand, modern technologies, such as, X-ray CT [6-11] [12] and

77 magnetic resonance imaging (MRI) [13], are developed to visualize the root system

78 architecture. For examples, root length data of the root system of 29-d old wheat plant

79 (*Triticum aestivum* L.) obtained by X-ray CT was compared with the data obtained using

80 flatbed scanner, demonstrating high correlation between them. Metzner et al. (2015)

81 examined the root system architecture of 23-d old bean plant (*Phaseolus vulgaris* L.) using

82 both X-ray CT and MRI and compared the data. In most of the previous studies, an industrial

83 CT scanner or a scanning system employing microfocus X-ray source is used, which is

84 suitable for routine analyses for the size of root systems of crop plants.

85   We have performed an experiment in the International Space Station 'Kibo' module

86 called "Space Seed" to understand effects of Earth's gravity on the entire life cycle of

4

87   Arabidopsis plants[14] and obtained dried root systems grown in rockwool slabs. For this

88   case, we have to deal with Arabidopsis root system which is composed of finer roots than

89   those of crop plant species as mentioned above as well as to distinguish the roots from

90   rockwool fibers having similar dimension to that of the roots. Therefore, we focused on

91   refraction-contrast X-ray micro-CT technique ,which is available at the beamline of the

92   synchrotron radiation facility SPring-8, because high brightness of nearly-parallel X-ray

93   beams enables imaging of samples at the micron scale [15]. In the present study, we tested

94   two different Hutches available at this beamline and aimed to optimize the observation

95   condition for the visualization of dried Arabidopsis root system developed in the rockwool

96   slab.

97

98   **Methods and materials**

99   **Plant materials and growth conditions**

100   The present experiment was performed during the preparation of the Space Seed experiment.

101   Growth conditions are basically the same as described previously [14], while the plant

102   materials and the employed instrument were as follows. Twenty-four seeds of Arabidopsis

103   (*Arabidopsis thaliana* (L.) Heynh.) Landsberg *erecta* (Ler) were sterilized and sown on a

104   rockwool slab (W × D × H = 50 × 42 × 10 mm) (Nichias Corp, Tokyo, Japan) using gum

105   arabic and germinated in a polycarbonate growth chamber having the outer dimensions of W

106   × D × H = 60 × 50 × 60 mm and the dimensions of its inner void space was W × D × H = 56

107   × 46 × 48 mm (Fig. 1). The rockwool slab was covered with a transparent plastic plate and

108   growth chambers were installed in the prototype of the Plant Experimental Units, which was

109   designed for experiments in the International Space Station [14]. Plants were illuminated

110   laterally with LED matrix [16] and light intensity was 29 μmol m^{-2} s^{-1} when measured at the

111   bottom center of the growth chamber. Plants used for the following experiment were grown

112 for 46 days and the rockwool slabs were dried and the shoot system of the plants was

113 removed before the observation. Typical plants during its development are shown in Fig. 1.

114

115 **Refraction contrast X-ray micro-CT**

116 Refraction contrast X-ray micro-CT was performed at the experimental hutches (Hutch 1 and

117 3), where different spatial resolutions are available, of the beamline BL20B2 of the SPring-8

118 synchrotron radiation facility at Japan Synchrotron Radiation Research Institute, according

119 basically to the method described by Karahara et al. [17]. Its experimental setup is shown in

120 Fig. 2 and a brief of the method is as follows. The Hutch 1 and 3 are located 42 m and 206 m,

121 respectively, from the bending magnet X-ray source. The X-ray energy was adjusted to 25

122 keV. The images consecutively projected on the fluorescent screen were recorded by a CMOS

123 camera (ORCA-Flash 4.0; Hamamatsu Photonics KK, Hamamatsu, Japan) (Fig. 2a). The

124 image sizes obtained at the Hutch 1 and Hutch 3 were 2048 × 2048 pixels (ca. 5 × 5 mm) and

125 2048 × 556 pixels, (ca. 50 × 15 mm), respectively. A series of 900 and 3000 projections were

126 recorded over 180 degree for Hutch 1 and 3 observation, respectively. Because thickness of

127 the rockwool slab was 10 mm, observation was separately done for the upper and lower

128 halves for Hutch 1 observation. The spatial (pixel) resolution of the 3-D structure was

129 estimated to be 25.5 µm pixel^{-1} for the Hutch 3 data, and 2.76 µm pixel^{-1} for the Hutch 1 data,

130 respectively. The convolution back projection method was used for tomographic

131 reconstruction [18] (Fig. 3b). To determining optimal filter used for reconstruction, Chesler,

132 Ram-Lak, and Shepp-Logan filter, which are provided by the software package SP-µCT

133 (http://www-bl20.spring8.or.jp/xct/), were tested and the results were compared from the

134 aspect of background noises and clarity of root boundaries. Tomographic slices were obtained

135 and 3-D models (isosurface, wireframe) were drawn using the IMOD software package [19],

6

136 as previously described [20]. Volume models were drawn using the software UCSF Chimera

137 (https://www.cgl.ucsf.edu/chimera/).

138

139 **Optical microscopy**

140 For microscopy of the cut surface of the root base and rockwool fibers, a multizoom

141 microscope (AZ100M, Nikon, Tokyo, Japan) equipped with a CMOS camera DS-Fi3 (Nikon,

142 Tokyo, Japan) was used.

143

144 **Results and discussion**

145 **Identification of individual roots in a tomographic slice obtained by the observation at**

146 **Hutch 3**

147 After removing the shoot (upper) part of the plant, we identified positions of the plants under

148 a multizoom microscope, finding cut surfaces of root or hypocotyl of the plants. Referring the

149 position of the plant on the micrograph (Fig. 4a and b), we identified the root in a

150 tomographic slice (Fig. 4c). Cross section of a root (or hypocotyl) often appeared ring-shape

151 in a transverse tomographic slice because large cavity is often formed inside the root possibly

152 when the plant was completely dried (Fig. 4c). The root system of Arabidopsis is a taproot

153 system and is mainly composed of the primary root as the taproot and the secondary root as

154 the lateral root. Shape of a primary root grown vertically downward in the rockwool slab was

155 visualized in a longitudinal tomographic slice (Fig. 4d).

156   Next, we compared the appearance of the root in transverse tomographic slices

157 when three different filters, Chesler, Ram-Lak, and Shepp-Logan filter were used during

158 tomographic reconstruction. When reconstructed using Chesler filter in the case of data

159 obtained at Hutch 3, background noise was reduced while root boundary became obscure

160 (Fig. 4e). When reconstructed using Ram-Lak and Shepp-Logan filter, root boundary

7

161   appeared clearer compared with Chesler. However, because Ram-Lak filter gives root

162   boundary smoother than Shepp-Logan filter (Fig. 4g) when carefully compared between

163   them, we have finally chosen to use Ram-Lak filter (Fig. 4f).

164

165   **Three-dimensional volume imaging of an individual root by the observation at Hutch 3**

166   Shapes of the roots were roughly visualized by automatically drawing of isosurface (volume)

167   models based on the voxel value (Fig. 5a and b). A considerable amount of fibrous and

168   particulate fragmentary structures, which are due to component materials of the rockwool,

169   were observed around the root besides the root itself (Fig. 5a and b). Some of these structures

170   could be removed using "Delete small pieces" function of the isosurface command of IMOD

171   software (Fig. 5c).

172   Isosurface models change depending on the threshold level, above which all voxels

173   are enclosed by the surface. For a quantitative approach, it is necessary to find out the

174   appropriate threshold level. The actual cross-sectional area of the root at its cut surface was

175   measured first (Fig. 6a). Then the cross-sectional areas of the isosurface models were

176   measured at the same position as of Fig. 6a when the threshold level was changed from 70 to

177   76 (Fig. 6b-g). In this case, the closest value was achieved when the threshold level was 73.

178   Therefore, we can conclude that the isosurface model closest to the actual root is the one

179   demonstrated in Fig. 6f.

180   However, even if the threshold level is fixed at the most appropriate value,

181   unexpected connections between the root and surrounding rockwool materials were frequently

182   observed. Also, unexpected disconnection of signals of the root occurred due to local

183   attenuation of signals possibly at the thinner part of the root. These problems made it difficult

184   to construct a 3D model of an entire root system only by making an isosurface model at one

185   representative threshold value.

8

186   Instead, 3D wireframe models of roots were made, which is useful to measure the

187 root length as well as to obtain other parameters representing morphology of roots, such as

188 tortuosity, by manually tracing the signal of the root from the base toward the tip,

189 simultaneously referring isosurface models adjusting around the appropriate threshold level

190 (Fig. 7).

191   Nevertheless, in many cases, unexpected disconnection of signals of the root

192 frequently occurred, which made it difficult to trace entire part particularly of the secondary

193 roots only by using Hutch 3 data. Therefore, we also tested Hutch 1 which enabled

194 observation at higher spatial resolution.

195

196 **Observation of roots at higher spatial resolution at Hutch 1**

197 In the case of data obtained at Hutch 1 where background noises were more noticeable (Fig.

198 8d and e), Chesler filter was used during tomographic reconstruction. Appearance of the

199 transverse sections of the root is much clear in the tomographic slices of a reconstruction

200 obtained by the observation at Hutch 1 (Fig. 8d and e) when compared with those obtained by

201 the observation at Hutch 3 (Fig. 8a and b). Cavity formed inside the root can be clearly seen

202 in the slice of the Hutch 1 reconstruction (Fig. 8d and e). An isosurface model of the root is

203 much clearer when using the data obtained at Hutch 1 (Fig. 8f) than the data obtained at

204 Hutch 3 (Fig. 8c). Rockwool fibers around the root were separated from the root and can be

205 clearly seen by isosurface modeling using Hutch 1 reconstruction (Fig. 8f) although they were

206 not separated from the root and coalesced into an agglomerated structure by isosurface

207 modeling using Hutch 3 reconstruction (Fig. 8c).

208   Observation at Hutch 1 revealed detailed structures of the secondary root and

209 component materials of the rockwool. The secondary root, which is generally thinner than the

210 primary root, and rockwool fibers were distinguished by isosurface modeling using Hutch 1

211   data (Fig. 9b) while those structures were agglomerated in that of Hutch 3 (Fig. 9a). A fibrous

212   form of rockwool observed in the Hutch 3 reconstruction does neither appear to be straight

213   nor smooth but has an amorphous shape (Fig. 9a). On the other hand, a fiber observed in the

214   Hutch 1 reconstruction appears to be straight and smooth (Fig. 9b and d) which is close to its

215   shape observed under a multizoom microscope (Fig. 9e), indicating that the fibers recognized

216   in the Hutch 1 data are considered to be individual fibers. Thickness of the isosurface model

217   of the secondary root and a fibrous form of rockwool was measured and compared between in

218   Hutch 3 and in Hutch 1 reconstructions (Table 1). As a result, thickness of a fibrous form of

219   rockwool measured using the isosurface models of Hutch 3 data (78.0 ± 2.6 μm) was

220   considerably thicker than that of Hutch 1 data (13.3 ± 0.1 μm), suggesting that a fibrous form

221   of rockwool observed at Hutch 3 is considered to be a bundle of single rockwool fibers. And

222   thickness of a fibrous form of a rockwool measured using the isosurface models of Hutch 3

223   data (78.0 ± 2.6 μm) was even thicker than the thickness of the secondary root measured

224   using the isosurface models of Hutch 3 data (60.2 ± 7.6 μm), suggesting that this makes

225   difficult to distinguish between the secondary root and a bundle of rockwool fibers in some

226   cases. Thickness of a single rockwool fiber measured using the isosurface models of Hutch 1

227   data (13.3 ± 0.1 μm) was still thicker than its actual size measured using optical micrographs

228   (9.1 ± 0.1 μm). Nevertheless, the isosurface model of a fibrous form of rockwool made using

229   Hutch 1 data is considered to be a single fiber because its thickness (13.3 ± 0.1 μm) is still

230   smaller than the twice of the thickness measured using optical micrographs (9.1 ± 0.1 μm).

231   This result is comparable to, or even slightly higher than, the spatial resolution (voxel size, 28

232   μm) realized in the previous study done by Metzner et al. (2015) using Fraunhofer

233   Development Center X-ray Technology (EZRT). As a result, the secondary roots could be

234   successfully traced for the longer distance using Hutch 1 data than the Hutch 3 data due to

235   higher spatial resolution (Fig. 10).

10

236   In addition to the rockwool fibers, globular structures called 'shot' , which was

237   formed during the manufacturing of rockwool slabs [21], were clearly observed in a

238   tomographic slice (Fig. 9c) as well as in isosurface models (Fig. 9d) of Hutch 1. These

239   globular structures were also found in isosurface rendering (Fig. 4d) or in a tomographic slice

240   (Fig. 5a) obtained using Hutch 3 data. Optical microscopy revealed a 'shot' structure as well as

241   the material agglutinating rockwool fibers called 'binder', which is composed of resin and has

242   amorphous structure (Fig. 9e). Existence of these component materials of rockwool slabs also

243   made it difficult to distinguish the secondary root in the rockwool slab using Hutch 3 data

244   particularly when the roots became thinner.

245   Figure 11 shows volume models of the root system made by using the volume

246   viewer of UCSF Chimera adjusting the visible range of voxel value. In both cases of Hutch 3

247   and Hutch 1 data, structures related to the rockwool, such as globular ones, are visible in the

248   broad configuration of visible range of voxel value (Fig. 11 a, c, and e) while morphology of

249   the root system is more clearly visible in the narrow configuration (Fig. 11 b, d, and f).

250   Globular structures have mostly disappeared particularly in the case of narrow configuration

251   of Hutch 1 data (Fig. 11d and f). These results indicate that the materials of rockwool slabs

252   have more opacity to X-ray, or, absorb more X-ray than the materials of the root.

253   The limit for the smallest observable root is a function of the quality of the image

254   (signal-to-noise ratio) and resolution [6]. The smallest observable object is generally

255   considered to be of a size of twice the spatial resolution and this may even not be sufficient if

256   the image is noisy and background is not homogeneous [22]. In other words, the smallest

257   observable object should be larger than 2 pixels / voxels. Because effective pixel size of

258   Hutch 3 data is 25.5 μm pixel^{-1} and that of Hutch 1 data is 2.76 μm pixel^{-1}, respectively,

259   expected size of the smallest observable object is likely to be 51 μm pixel^{-1} and 5.52 μm

260   pixel^{-1}, respectively. Average size of the isosurface model of the secondary root made using

11

261   Hutch 3 data was 60.2 μm (Table 1), which is comparable to the expected size of the smallest

262   observable object at Hutch 3 (51 μm pixel^{-1}). Even at this level, the spatial resolution, which

263   is realized in the present system, is higher than the previous studies mentioned in the

264   Introduction using an industrial CT scanner or a scanning system using microfocus X-ray

265   source.

266   We can conclude that the spatial resolution of the observation at Hutch 1 is high

267   enough to distinguish each rockwool fiber. Considering the difference between the actual

268   thickness of the rockwool fiber (9.1 μm) and that of its isosurface model (13.3 μm), the actual

269   thickness of the secondary root should be smaller than that of its isosurface model (20.9 μm).

270   Further, it should be noted that dried roots analyzed in the present study had become thinner

271   than those before drying.

272   A wireframe model of the root system drawn using Hutch 1 data demonstrated more

273   extended architecture of the secondary roots as well as the primary root (Fig. 10b). On the

274   other hand, that of Hutch 3 data demonstrated only the basal parts of the secondary roots

275   while the architecture of the primary root was visualized entirely (Fig. 10a). Nevertheless,

276   Hutch 3 data are useful because these provide an overview map for roughly comparing the

277   growth of roots as well as for selecting individual roots for further detailed analyses of actual

278   specimens of the Space Seed experiment. Together, precise determination of the minimum

279   thickness of the secondary root observable remains to be done for that study.

280

281   **Conclusions**

282   We can conclude that the spatial resolution of the observation at Hutch 1 is high enough to

283   distinguish individual rockwool fibers as well as the secondary roots having the thickness of

284   its isosurface model at 20.9 μm on the average. This enabled us to distinguish between them

285   and to trace the architecture of the Arabidopsis root system including the secondary roots as

12

286   well as the primary root. In addition, the observation at Hutch 3 provides an overview map of

287   the root system grown in the rockwool slab for the purpose of screening of specimens for

288   further detailed analyses of individual root systems.

289

301

302   **References**

303

304   1.   O'toole J C and Bland W L (1987) Genotypic variation in crop plant root systems. *Adv.*

305   *Agron.* 41: 91-145.

306   2.   Tran T T, Kano-Nakata M, Suralta R R, Menge D, Mitsuya S, Inukai Y and Yamauchi A

307   (2015) Root plasticity and its functional roles were triggered by water deficit but not by

308   the resulting changes in the forms of soil N in rice. *Plant Soil* 386: 65-76.

309   3.   Kano M, Inukai Y, Kitano H and Yamauchi A (2011) Root plasticity as the key root trait

310   for adaptation to various intensities of drought stress in rice. *Plant Soil* 342: 117-128.

311   4.   Kano-Nakata M, Inukai Y, Wade L J, Siopongco J D L C and Yamauchi A (2011) Root

312   development, water uptake, and shoot dry matter production under water deficit

313   conditions in two CSSLs of rice: Functional roles of root plasticity. *Plant Prod. Sci.* 14:

314   307-317.

315   5.   Faget M, Nagel K A, Walter A, Herrera J M, Jahnke S, Schurr U and Temperton V M

316   (2013) Root–root interactions: extending our perspective to be more inclusive of the

317   range of theories in ecology and agriculture using in-vivo analyses. *Ann. Bot. (Lond.)*

318   112: 253-266.

319   6.   Flavel R J, Guppy C N, Tighe M, Watt M, Mcneill A and Young I M (2012) Non-

320   destructive quantification of cereal roots in soil using high-resolution X-ray tomography.

321   *J. Exp. Bot.* 63: 2503-2511.

322   7.   Rogers E D, Monaenkova D, Mijar M, Nori A, Goldman D I and Benfey P N (2016) X-

323   ray computed tomography reveals the response of root system architecture to soil texture.

324   *Plant Physiol.* 171: 2028-2040.

325   8.   Mairhofer S, Zappala S, Tracy S, Sturrock C, Bennett M J, Mooney S J and Pridmore T P

326   (2013) Recovering complete plant root system architectures from soil via X-ray μ-

327   computed tomography. *Plant Methods* 9: 1-7.

328   9.   Daly K R, Tracy S R, Crout N M J, Mairhofer S, Pridmore T P, Mooney S J and Roose T

329   (2018) Quantification of root water uptake in soil using X-ray computed tomography and

330   image-based modelling. *Plant Cell Environ.* 41: 121-133.

331 10. Gao W, Schlüter S, Blaser S R G A, Shen J and Vetterlein D (2019) A shape-based

332   method for automatic and rapid segmentation of roots in soil from X-ray computed

333   tomography images: Rootine. *Plant Soil* 441: 643-655.

334 11. Yoshida Y, Arita T, Otani J and Sawa S (2020) Visualization of Toyoura sand-grown

335   plant roots by X-ray computer tomography. *Plant Biotechnol. (Tokyo)* 37: 481-484.

14

336 12. Teramoto S, Takayasu S, Kitomi Y, Arai-Sanoh Y, Tanabata T and Uga Y (2020) High-

337   throughput three-dimensional visualization of root system architecture of rice using X-ray

338   computed tomography. *Plant Methods* 16: 1-14.

339 13. Metzner R, Eggert A, Van Dusschoten D, Pflugfelder D, Gerth S, Schurr U, Uhlmann N

340   and Jahnke S (2015) Direct comparison of MRI and X-ray CT technologies for 3D

341   imaging of root systems in soil: potential and challenges for root trait quantification.

342   *Plant Methods* 11: 1-11.

343 14. Karahara I, Suto T, Yamaguchi T, Yashiro U, Tamaoki D, Okamoto E, Yano S, Tanigaki

344   F, Shimazu T, Kasahara H, Kasahara H, Yamada M, Hoson T, Soga K and Kamisaka S

345   (2020) Vegetative and reproductive growth of Arabidopsis under microgravity conditions

346   in space. *J. Plant Res.* 133: 571-585.

347 15. Karahara I, Yamauchi D, Uesugi K and Mineyuki Y (2015/4) Three-dimensional imaging

348   of plant tissues using X-ray micro-computed tomography. *Plant Morphol.* 27: 21-26.

349 16. Yano S, Kasahara H, Masuda D, Tanigaki F, Shimazu T, Suzuki H, Karahara I, Soga K,

350   Hoson T, Tayama I, Tsuchiya Y and Kamisaka S (2013) Improvements in and actual

351   performance of the Plant Experiment Unit onboard Kibo, the Japanese experiment

352   module on the international space station. *Adv. Space Res.* 51: 780-788.

353 17. Karahara I, Umemura K, Soga Y, Akai Y, Bando T, Ito Y, Tamaoki D, Uesugi K, Abe J,

354   Yamauchi D and Mineyuki Y (2012) Demonstration of osmotically dependent promotion

355   of aerenchyma formation at different levels in the primary roots of rice using a

356   "sandwich" method and X-ray computed tomography. *Ann. Bot. (Lond.)* 110: 503-509.

357 18. Uesugi K, Hoshino M, Takeuchi A, Suzuki Y, Yagi N and Nakano T (2010)

358   Development of fast (sub-minute) micro-tomography. *AIP Conf. Proc.* 1266: 47-50.

359 19. Kremer J R, Mastronarde D N and Mcintosh J R (1996) Computer visualization of three-

360   dimensional image data using IMOD. *J. Struct. Biol.* 116: 71-76.

15

20. Karahara I, Suda J, Tahara H, Yokota E, Shimmen T, Misaki K, Yonemura S, Staehelin L A and Mineyuki Y (2009) The preprophase band is a localized center of clathrin-mediated endocytosis in late prophase cells of the onion cotyledon epidermis. *Plant J.* 57: 819-831.

21. Kitahara H (2015) Filamentation technology of rock wool. *Nichias Technol. Rev.* 368: 1-5.

22. Kaestner A, Schneebeli M and Graf F (2006) Visualizing three-dimensional root networks using computed tomography. *Geoderma* 136: 459-469.

Figure legends

Fig. 1. Pictures of typical Arabidopsis plants grown on a rockwool slab in a polycarbonate growth chamber. (a) Plants on Day 12. Rosette leaves are growing. Surface of the rockwool slab is seen underneath the plants. (b) Plants on Day 32. Flowers are forming. Internal length of the front side of the chamber is 46 mm. Red arrowheads indicate the rockwool slabs.

Fig. 2. Experimental set up of the beamline BL20B2. A broken arrow (a) indicates the X-ray path in the Hutch 3. A rockwool slab placed on a rotation stage in the Hutch 3 (b) or the Hutch 1 (c). Seeds of morning glory were placed on the rockwool slabs as position markers.

Fig. 3. Two-dimensional projection of refraction contrast image of the rockwool slab (side view) (a) and a transverse tomographic slice of the rockwool slab (b). Scale bars = 1 cm.

386   **Fig. 4.** Identification of individual roots in a tomographic slice. (a) A multizoom micrograph

387   of an entire rockwool slab. A red rectangle shows the area magnified in (b). A white dashed

388   line shows the position from where the longitudinal tomographic slice shown in (d) was

389   obtained. (b) A magnified microscopic view showing a cut surface of the base of the root

390   found on the surface of the rockwool slab (red arrowhead). A dark-brown round-shape thing

391   located nearby is a released seed coat, which frequently helps to find the position of the root.

392   (c) A transverse tomographic slice showing the same position as shown in (b).White ring-

393   shape object (red arrowhead) shows the cross section of the root. (d) A longitudinal

394   tomographic slice obtained at the position indicated in (a) demonstrating longitudinal

395   continuity of a primary root (red arrowheads). (e) – (g) Comparison of the tomographic slices

396   reconstructed using different filters. (e) Chesler. (f) Ram-Lak. (g) Shepp-Logan. (c) and (d)

397   are actually made using Chesler filter. Scale bars = 1 cm (a), 1 mm [(b) – (d)].

398

399   **Fig. 5.** Three-dimensional volume imaging of individual root and determining its threshold.

400   (a) A volume model made by using Volume Viewer of UCSF Chimera. (b) An isosurface

401   model made by using isosurface command of IMOD software. (c) The same region

402   where "Delete small pieces" function of the isosurface command of IMOD software was

403   applied. Scale bars = 1 mm.

404

405   **Fig. 6.** Finding the appropriate threshold level for isosurface rendering of the root. (a) A

406   magnified multizoom micrograph showing the cut surface of the base of a root. A closed

407   contour drawn in red shows the boundary of the root surface (arrowhead). The value is the

408   actual cross-sectional area of the root surrounded by the contour. (b), (c), and (d) Cross

409   sections of the isosurface models of the same root as shown in (a) (arrowheads) and their

410   cross-sectional area values at the same position as shown in (a). (e), (f), and (g) Lateral views

411 of the isosurface rendering which correspond to (b), (c), and (d), respectively. The threshold

412 level was changed from 70 (b) and (e), 73 (c) and (f), to 76 (d) and (g). Scale bars = 200 μm

413 [(a) – (d)], 1 mm [(e) – (g)].

414

415 **Fig. 7.** Making wireframe models of roots. (a) Lateral view of an isosurface model of the

416 basal part of the root. Upper or lower red cuboid indicates the region shown in (b) or (d),

417 respectively. (b) and (d) Transverse views of isosurface models from above corresponding to

418 the regions indicated in (a). (c) and (e) Transverse tomographic slices at the positions

419 corresponding to the regions indicated in (b) and (d), respectively. Green arrowheads show

420 the primary root. Blue arrowheads show the secondary root. (f) A wireframe models of roots.

421 Green contour shows the primary root. Blue contours show the secondary root. Scale bars = 1

422 mm.

423

424 **Fig. 8.** Comparison of the observations of the same root between Hutch 3 and Hutch 1. (a)

425 and (b) Transverse tomographic slices obtained by the observation at Hutch 3. Effective pixel

426 size = 25.5 μm pixel^{-1}. (d) and (e) Transverse tomographic slices obtained by the observation

427 at Hutch 1. Effective pixel size = 2.76 μm pixel^{-1}. Red arrowheads show the transverse views

428 of the root. (a) and (d) Transverse tomographic slices, which shows a thicker part of the

429 primary root, obtained near the base of the root. (b) and (e) Transverse tomographic slices,

430 which shows a thinner part of the primary root with a secondary root (white arrow heads),

431 obtained at 4.6 mm below the base of the root. (c) and (f) Isosurface models using data

432 obtained at Hutch 3 (c) or Hutch 1 (f). Red arrowheads show the base of the root. Scale bars =

433 200 μm.

434

18

435 **Fig. 9.** Detailed structures of the root and component materials of the rockwool revealed by

436 the observation at Hutch 1. (a) and (b) Isosurface models of a fibrous form of rockwool and

437 the secondary root obtained by the observation at Hutch 3 (effective pixel size is 25.5 μm

438 pixel^{-1}) (a) and Hutch 1 (effective pixel size is 2.76 μm pixel^{-1}) (b), respectively. Blue open

439 contours show wireframe models of the secondary roots. (c) and (d) A transverse tomographic

440 slice (c) and its corresponding isosurface model (d) showing a globular shot structure of

441 rockwool (arrowheads). (e) A multizoom micrograph showing an actual globular shot

442 structure of rockwool (red broken circle) and 'binder' material agglutinating rockwool fibers

443 (blue rectangular). Scale bars = 200 μm.

444

445 **Fig. 10.** Comparison of wireframe models of the same root system drawn using Hutch 3 (a)

446 and Hutch 1 (b) data. (c) Four root system models are seen in the wider view of the Hutch 3

447 data. Green contour shows the primary root. A red arrowhead shows the same root as in (a)

448 and (b). In (b) apical part of the primary root missing because this missing part was out of the

449 reconstructed volume data of the lower half. Blue contours show the secondary root. Scale

450 bars = 1 mm (a) and (b), 10 mm (c).

451

452 **Fig. 11.** Visualization of the root system by using the volume viewer of UCSF Chimera

453 adjusting the visible range of voxel value. (a) and (b) Volume models of the same root system

454 using Hutch 3 data when visualized in the broad (a) or narrow (b) visible range of voxel

455 value. (c) - (f) Volume models of the upper (c) and (d) or lower (e) and (f) part of the root

456 using Hutch 1 data when visualized in the broad (c) and (e) or narrow (d) and (f) visible range

457 of voxel value. Scale bars = 500 μm. (g) and (h) Examples of broad (g) or narrow (h)

458 configuration of the visible range of voxel value which were actually applied to visualize the

459 root volume model of (e) and (g) and (f) and (h), respectively. X axis shows voxel value. Y

19

460   axis shows frequency. Visible areas are filled in black. Histograms show distribution of voxel

461   values. Red line graphs show adjustment of opacity level.

462

463

464   **Table 1.** Comparison of the thickness of the secondary root and a fibrous form of rockwool

465   which was measured using the isosurface models of Hutch 3 and Hutch 1 as well as thickness

466   of a rockwool fiber measured using multizoom micrographs

467

| | Optical micrograph | | Isosurface model | | | |
| | | | Hutch 3 | | Hutch 1 | |
	Mean ± SE (μm)	n	Mean ± SE (μm)	n	Mean ± SE (μm)	n
Fibrous form of Rockwool	9.1 ± 0.1	35	78.0 ± 2.6	60	13.3 ± 0.1	60
The secondary root	ND		60.2 ± 7.6	8	20.9 ± 1.4	8

468   ND, not determined.

Fig. 1
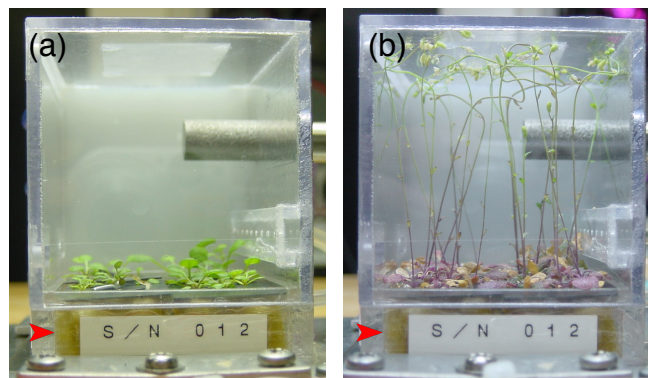
Fig. 1. Pictures of typical Arabidopsis plants grown on a rockwool slab in a polycarbonate growth chamber. (a) Plants on Day 12. Rosette leaves are growing. Surface of the rockwool slab is seen underneath the plants. (b) Plants on Day 32. Flowers are forming. Internal length of the front side of the chamber is 46 mm. Red arrowheads indicate the rockwool slabs.
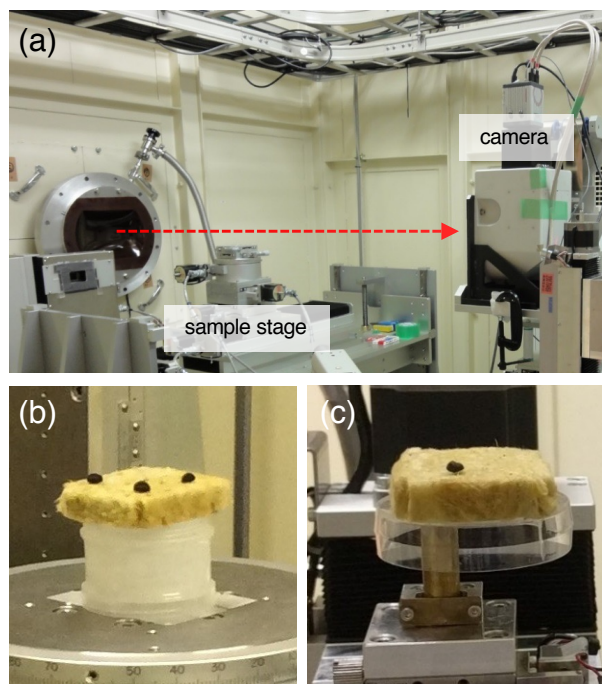
Fig. 2

Fig. 2. Experimental set up of the beamline BL20B2. A broken arrow (a) indicates the X-ray path in the Hutch 3. A rockwool slab placed on a rotation stage in the Hutch 3 (b) or the Hutch 1 (c). Seeds of morning glory were placed on the rockwool slabs as position markers.
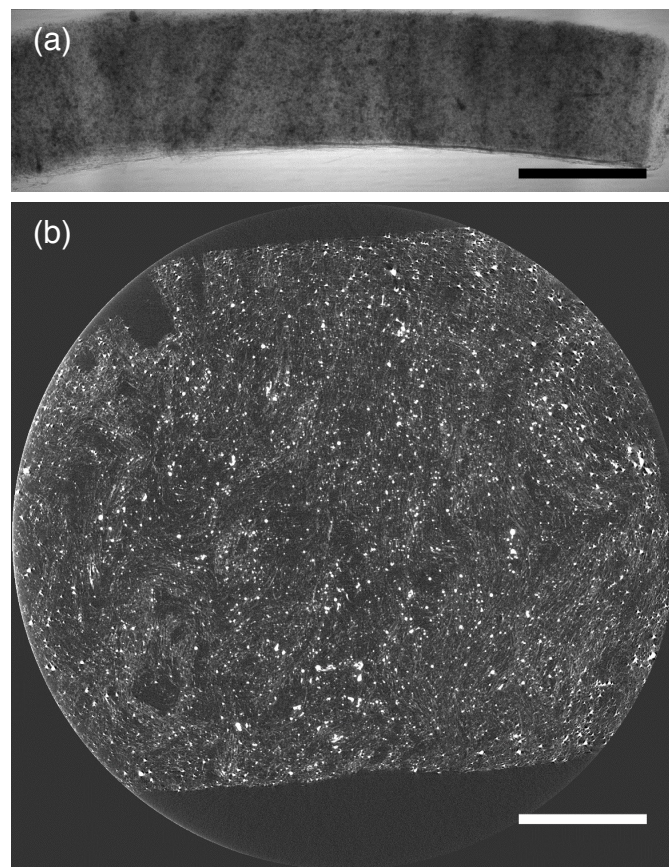
Fig. 3

Fig. 3. Two-dimensional projection of refraction contrast image of the rockwool slab (side view) (a) and a transverse tomographic slice of the rockwool slab (b). Scale bars = 1 cm.

Fig. 4
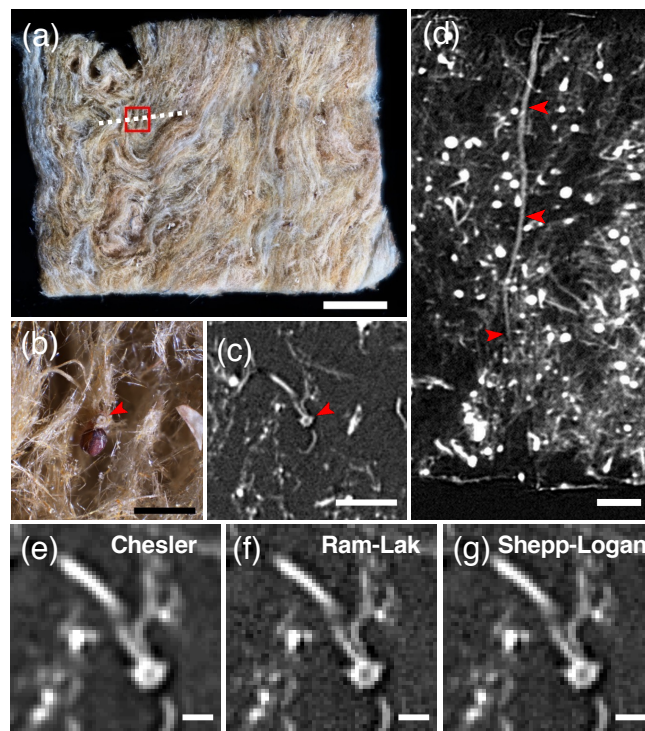
Fig. 4. Identification of individual roots in a tomographic slice. (a) A multizoom micrograph of an entire rockwool slab. A red rectangle shows the area magnified in (b). A white dashed line shows the position from where the longitudinal tomographic slice shown in (d) was obtained. (b) A magnified microscopic view showing a cut surface of the base of the root found on the surface of the rockwool slab (red arrowhead). A dark-brown round-shape thing located nearby is a released seed coat, which frequently helps to find the position of the root. (c) A transverse tomographic slice showing the same position as shown in (b).White ring-shape object (red arrowhead) shows the cross section of the root. (d) A longitudinal tomographic slice obtained at the position indicated in (a) demonstrating longitudinal continuity of a primary root (red arrowheads). (e) – (g) Comparison of the tomographic slices reconstructed using different filters. (e) Chesler. (f) Ram-Lak. (g) Shepp-Logan. (c) and (d) are actually made using Chesler filter. Scale bars = 1 cm (a), 1 mm [(b) – (d)].
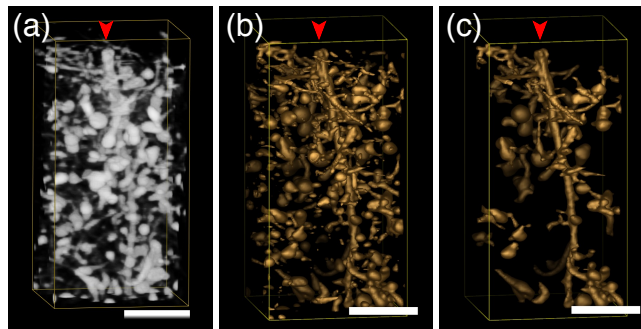
Fig. 5

Fig. 5. Three-dimensional volume imaging of individual root and determining its threshold. (a) A volume model made by using Volume Viewer of UCSF Chimera. (b) An isosurface model made by using isosurface command of IMOD software. (c) The same region where "Delete small pieces" function of the isosurface command of IMOD software was applied. Scale bars = 1 mm.
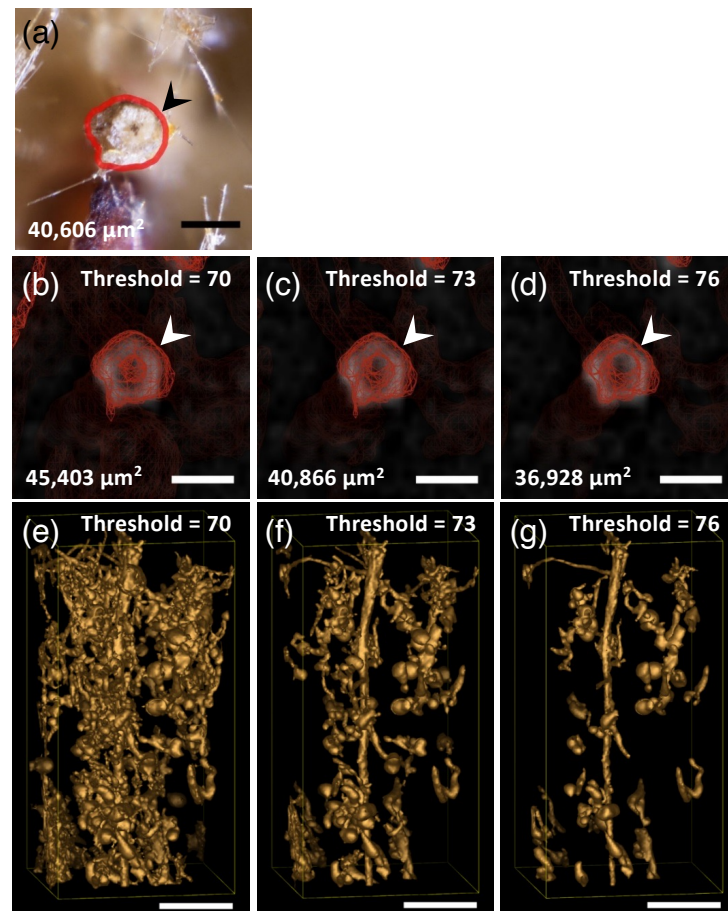
Fig. 6

Fig. 6. Finding the appropriate threshold level for isosurface rendering of the root. (a) A magnified multizoom micrograph showing the cut surface of the base of a root. A closed contour drawn in red shows the boundary of the root surface (arrowhead). The value is the actual cross-sectional area of the root surrounded by the contour. (b), (c), and (d) Cross sections of the isosurface models of the same root as shown in (a) (arrowheads) and their cross-sectional area values at the same position as shown in (a). (e), (f), and (g) Lateral views of the isosurface rendering which correspond to (b), (c), and (d), respectively. The threshold level was changed from 70 (b) and (e), 73 (c) and (f), to 76 (d) and (g). Scale bars = 200 μm [(a) – (d)], 1 mm [(e) – (g)].
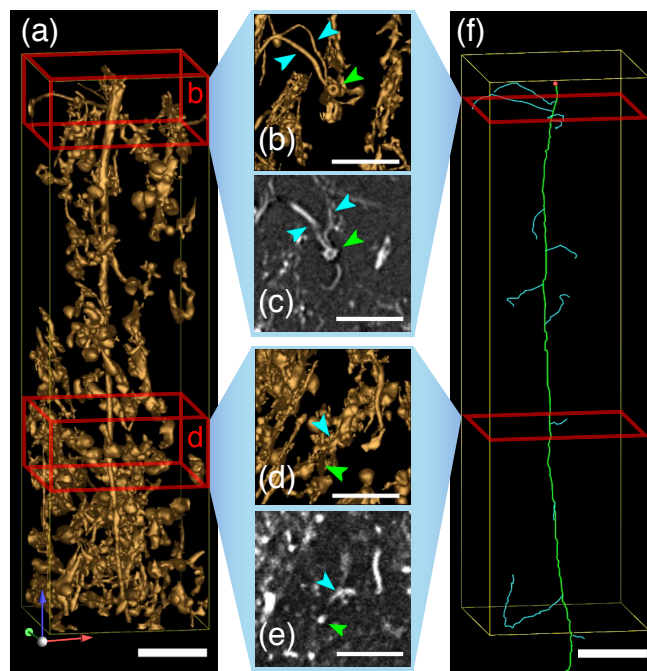
Fig. 7

Fig. 7. Making wireframe models of roots. (a) Lateral view of an isosurface model of the basal part of the root. Upper or lower red cuboid indicates the region shown in (b) or (d), respectively. (b) and (d) Transverse views of isosurface models from above corresponding to the regions indicated in (a). (c) and (e) Transverse tomographic slices at the positions corresponding to the regions indicated in (b) and (d), respectively. Green arrowheads show the primary root. Blue arrowheads show the secondary root. (f) A wireframe models of roots. Green contour shows the primary root. Blue contours show the secondary root. Scale bars = 1 mm.
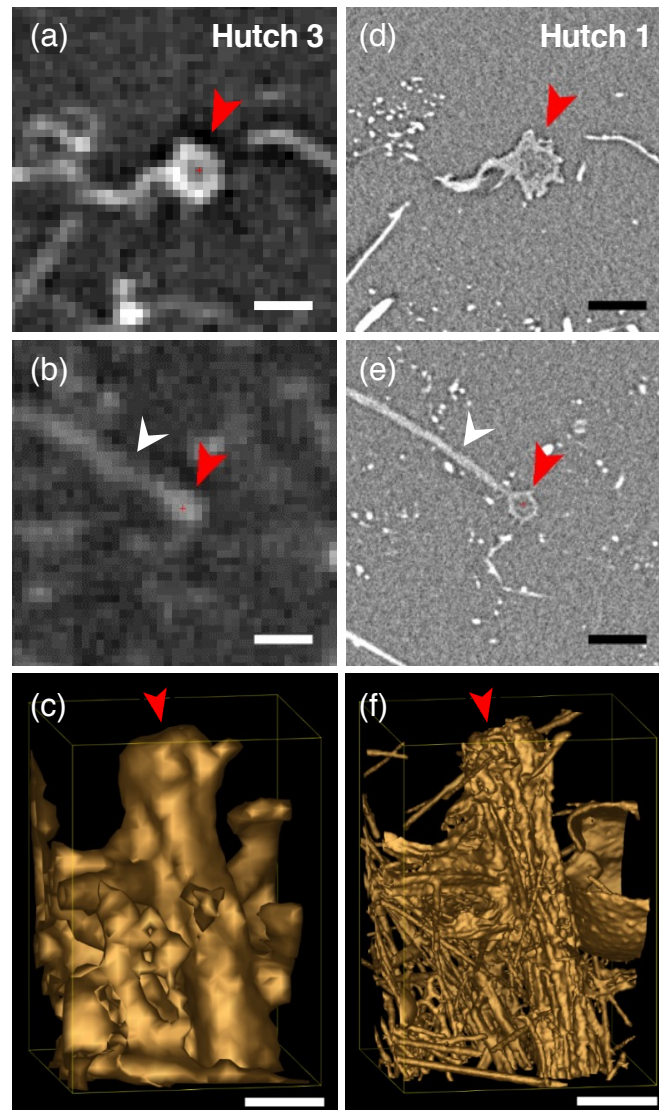
Fig. 8

Fig. 8. Comparison of the observations of the same root between Hutch 3 and Hutch 1. (a) and (b) Transverse tomographic slices obtained by the observation at Hutch 3. Effective pixel size = 25.5 µm pixel-1. (d) and (e) Transverse tomographic slices obtained by the observation at Hutch 1. Effective pixel size = 2.76 µm pixel-1. Red arrowheads show the transverse views of the root. (a) and (d) Transverse tomographic slices, which shows a thicker part of the primary root, obtained near the base of the root. (b) and (e) Transverse tomographic slices, which shows a thinner part of the primary root with a secondary root (white arrow heads), obtained at 4.6 mm below the base of the root. (c) and (f) Isosurface models using data obtained at Hutch 3 (c) or Hutch 1 (f). Red arrowheads show the base of the root. Scale bars = 200 µm.
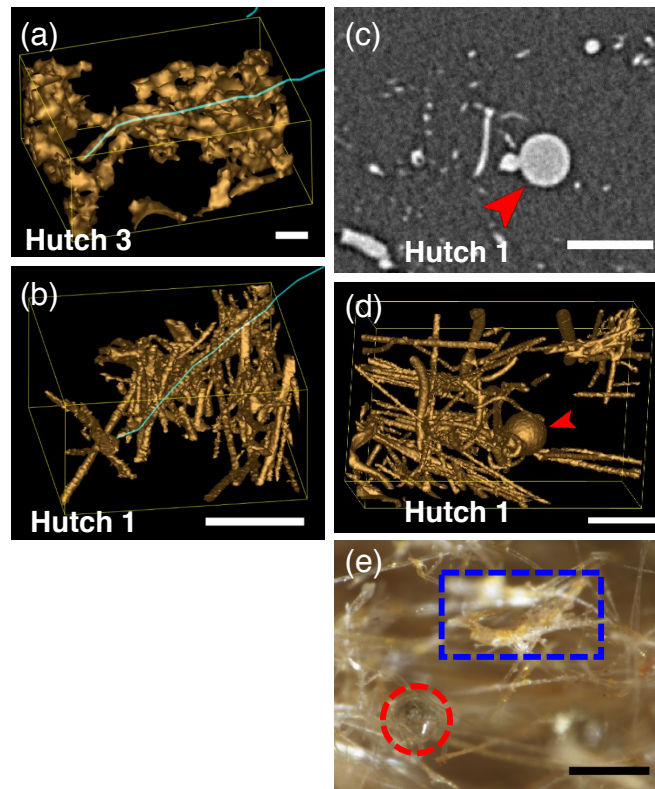
Fig. 9

Fig. 9. Detailed structures of the root and component materials of the rockwool revealed by the observation at Hutch 1. (a) and (b) Isosurface models of a fibrous form of rockwool and the secondary root obtained by the observation at Hutch 3 (effective pixel size is 25.5 µm pixel-1) (a) and Hutch 1 (effective pixel size is 2.76 µm pixel-1) (b), respectively. Blue open contours show wireframe models of the secondary roots. (c) and (d) A transverse tomographic slice (c) and its corresponding isosurface model (d) showing a globular shot structure of rockwool (arrowheads). (e) A multizoom micrograph showing an actual globular shot structure of rockwool (red broken circle) and 'binder' material agglutinating rockwool fibers (blue rectangular). Scale bars = 200 µm.
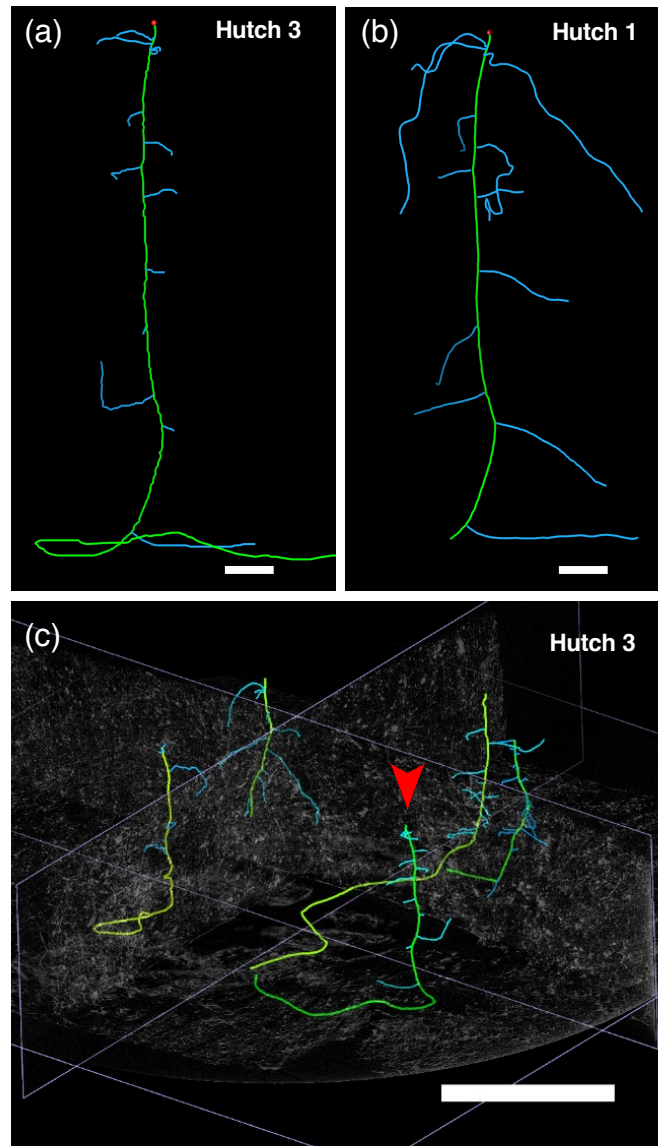
Fig. 10

Fig. 10. Comparison of wireframe models of the same root system drawn using Hutch 3 (a) and Hutch 1 (b) data. (c) Four root system models are seen in the wider view of the Hutch 3 data. Green contour shows the primary root. A red arrowhead shows the same root as in (a) and (b). In (b) apical part of the primary root missing because this missing part was out of the reconstructed volume data of the lower half. Blue contours show the secondary root. Scale bars = 1 mm (a) and (b), 10 mm (c).
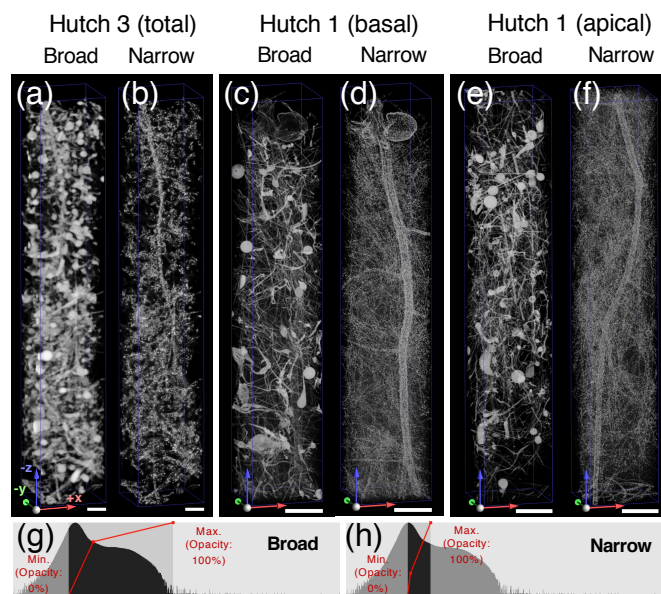
Fig. 11

Fig. 11. Visualization of the root system by using the volume viewer of UCSF Chimera adjusting the visible range of voxel value. (a) and (b) Volume models of the same root system using Hutch 3 data when visualized in the broad (a) or narrow (b) visible range of voxel value. (c) - (f) Volume models of the upper (c) and (d) or lower (e) and (f) part of the root using Hutch 1 data when visualized in the broad (c) and (e) or narrow (d) and (f) visible range of voxel value. Scale bars = 500 μm. (g) and (h) Examples of broad (g) or narrow (h) configuration of the visible range of voxel value which were actually applied to visualize the root volume model of (e) and (g) and (f) and (h), respectively. X axis shows voxel value. Y axis shows frequency. Visible areas are filled in black. Histograms show distribution of voxel values. Red line graphs show adjustment of opacity level.